

Dynamic Response Analysis of a Submerged Floating Tunnel under N Wave Action

Yipei Wang¹, Liushuai Cao¹, Ming He², Decheng Wan^{1*}

¹ Computational Marine Hydrodynamics Lab (CMHL), School of Naval Architecture, Ocean and Civil Engineering, Shanghai Jiao Tong University, Shanghai, China

² State Key Laboratory of Hydraulic Engineering Intelligent Construction and Operation, Tianjin University, Tianjin, China

*Corresponding Author

ABSTRACT

A submerged floating tunnel (SFT) is an underwater transportation structure designed for all-weather operation in deep-water environments. Although its submerged position reduces the impact of conventional waves, it remains vulnerable to extreme events such as tsunamis. This study applied the Smoothed Particle Hydrodynamics (SPH) method to analyze the hydrodynamic behavior of SFTs under tsunami-like N wave conditions. The fluid dynamics were governed by the continuity, momentum, and state equations, while the motion of the SFT was described by Newton's second law. The mooring system was modeled as massless, linear elastic springs. The convergence and accuracy of the SPH model were validated by numerically reproducing a laboratory experiment involving wave interactions with a moored floating structure. After validation, the SPH model was used to simulate the interactions between a representative N wave and an SFT with a circular cross-section shape (CSS), a buoyancy-weight ratio (BWR) of 1.3, and an inclined mooring angle (IMA) of 52.55°. The motion responses and mooring forces of the SFT were analyzed.

KEY WORDS: submerged floating tunnel; N-wave; motion response; computational fluid dynamics.

INTRODUCTION

A submerged floating tunnel (SFT), also known as an Archimedes Bridge, operates by balancing buoyancy, gravitational force, and mooring tension to remain positioned at a specific depth below the water surface. Its submerged location ensures that it neither obstructs maritime traffic nor is significantly affected by tidal fluctuation, conventional wave force, or ice coverage. Furthermore, the mooring system allows the SFT to be effectively deployed in deep waters and under varying geological conditions. While no SFTs have been built to date, several countries are actively exploring their potential for practical engineering applications (Faggiano *et al.* 2016; Kanie 2010; Larssen & Jakobsen 2010; Seo *et al.* 2015a).

Existing research has predominantly concentrated on the parameter design of SFTs under conventional wave conditions, with particular focus

on submergence depth, cross-sectional shape (CSS), buoyancy-weight ratio (BWR), and mooring configuration. Through theoretical analyses, Paik *et al.* (2004) investigated the effects of submergence depth on the coefficients of added mass, radiation damping, and wave excitation force of an SFT. Kunisu (2010) studied the influence of CSS on the drag and inertia forces acting on an SFT. By laboratory experiments, Seo *et al.* (2015a) identified significant lateral displacement of an SFT with a single vertical mooring system and suggested the adoption of a W-type double mooring system as an alternative. Yang *et al.* (2020) compared the motion characteristics of SFTs across varying submergence depths, BWRs, and inclined mooring angles (IMAs), proposing empirical equations to estimate SFT motion. Using numerical simulations, Chen *et al.* (2021) examined the influence of submergence depth and BWR on the kinematic response and mooring force of an SFT.

Fig. 1 illustrates three types of water-spanning structures: pier-supported or floating bridges above water, SFTs, and immersed tunnels. SFTs, stabilized by buoyancy, gravity, and mooring tension, avoid obstructing maritime traffic and are resilient to waves, tides, and ice. Their mooring systems enable use in deep waters and diverse geological conditions, unlike immersed tunnels.

Extreme disasters pose serious threats to marine structures. Therefore, it is essential to assess both the hydrodynamic behaviours of SFTs under conventional wave conditions and their safety in extreme scenarios. Fogazzi & Perotti (2000) studied the dynamic behaviour of an SFT under seismic excitation. Seo *et al.* (2015b) evaluated the global response of an SFT subjected to shock pressure by underwater explosion. Luo *et al.* (2019) simulated the collision between a submarine and an SFT, analysing the energy transfer among the water, the submarine, and the SFT. Xiang *et al.* (2018) investigated the dynamic responses of SFTs during sudden mooring system failures, identifying key factors influencing the mooring-breakage stage.

A tsunami is a gravity wave resulting from the sudden displacement of a large volume of water caused by rapid changes in the equilibrium position of a water body. These massive waves are typically triggered by seismic activity, volcanic eruptions, landslides, or any other vertical disturbance within a water body. Tsunami waves are characterized by exceptionally long wavelengths and exhibit significant nonlinearity,

particularly when propagating through the relatively shallow waters of the continental shelf. Due to their highly destructive nature, it is critical to study the hydrodynamic responses of marine structures to tsunami waves. However, to the best of our knowledge, the specific interactions between N waves and SFTs have not yet been investigated.

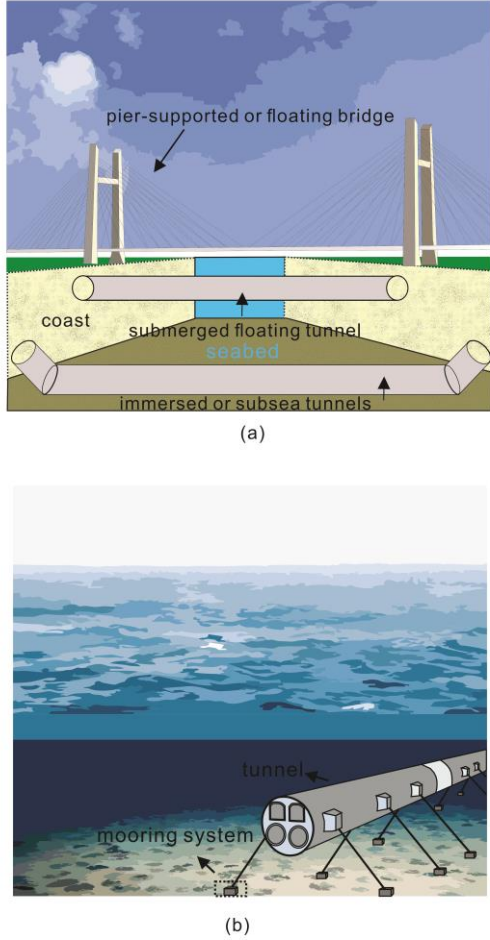


Fig. 1. Illustrations of water-spanning transportation structures with a focus on the SFT.

Simulating tsunami waves has long been a challenging task, both in laboratory experiments and numerical simulations. Researchers have typically relied on solitary waves or N waves to approximate the modeling of tsunami waves. However, recent studies have raised concerns about the accuracy of using solitary waves to simulate tsunamis (Madsen 2008; Chan & Liu, 2012). The primary issue is that the initial tsunami wave, when approaching the shore, often manifests as either a leading depression or a leading elevation, which a solitary wave cannot accurately represent. In contrast, N waves are better able to capture this phenomenon. However, relatively little work has been done on generating N waves in laboratory experiments or simulating them numerically. Goseberg et al. (2013) developed an innovative approach utilizing high-capacity, loop-controlled pipeline pumps to facilitate long-wave generation, significantly enhancing the ability to simulate tsunamis. Likewise, Lima et al. (2019) successfully generated N waves in laboratory conditions using a piston-type wavemaker. In numerical wave generation, Zhang et al. (2024) employed the piston-type wavemaker method to generate N waves in an SPH-based wave tank.

To effectively capture the interaction between N wave and SFTs, this study employs the Smoothed Particle Hydrodynamics (SPH) method to solve the Navier-Stokes equations. Widely utilized in marine engineering, The mesh-free and Lagrangian characteristics of SPH make it particularly well-suited for handling moving solid boundaries and free surface flows without mesh distortion, thereby enabling efficient capture of the complex behaviors involved in N wave interactions with SFTs.

The remainder of this paper is structured as follows: Firstly, the SPH model is introduced. Then, the convergence and accuracy of the model are validated. Following that, the hydrodynamic behavior of the SFT under N wave action is analyzed. Subsequently, the effects of structural parameters are investigated. Finally, the key conclusions are summarized.

SPH MODEL

A numerical model based on the SPH method is established to simulate wave interactions with a moored floating structure. This section outlines the governing equations for fluid dynamics, the motion equations of the structure, and the time-stepping scheme.

Governing Equations for Fluid Dynamics

The SPH method is generally categorized into Weakly Compressible SPH (WCSPH) and Incompressible SPH (ISPH). In WCSPH, the governing equations for fluid dynamics, consisting of the continuity and momentum equations, can be discretized as follows (Antuono et al. 2010):

$$\frac{D\rho_i}{Dt} = -\rho_i \sum_j (\mathbf{u}_j - \mathbf{u}_i) \cdot \nabla_i W_{ij} V_j + \delta h c_0 \sum_j \Psi_{ij} \cdot \nabla_i W_{ij} V_j \quad (1)$$

$$\frac{D\mathbf{u}_i}{Dt} = -\frac{1}{\rho_i} \sum_j (p_j + p_i) \nabla_i W_{ij} V_j + \mathbf{g} + \alpha h c_0 \frac{\rho_0}{\rho_i} \sum_j \pi_{ij} \nabla_i W_{ij} V_j \quad (2)$$

Here, subscripts i and j denote the target and neighbouring particles, respectively. t is the time. ρ , p , V , \mathbf{u} , and \mathbf{r} are the density, the pressure, volume, velocity, and position, respectively; $\rho_0 = 1000 \text{ kg/m}^3$ is the reference density. \mathbf{g} is the gravitational acceleration. W is the Wendland C2 kernel function (Wendland 1995). $h = 1.5\delta_p$ is the smoothing length, where δ_p is the initial particle spacing. $c_0 = 10(|\mathbf{g}|d)^{1/2}$ is the numerical speed of sound (He et al. 2019), where d is the water depth. $\delta = 0.1$ is the diffusive coefficient. $\alpha = 8\nu/(hc_0)$ is the artificial viscosity coefficient, where ν is the kinematic viscosity.

In Equation (1), Ψ_{ij} is a numerical diffusive term for smoothing the pressure field, given by

$$\Psi_{ij} = 2 \left[(\rho_j - \rho_i) - \frac{1}{2} (\langle \nabla \rho \rangle_j^L + \langle \nabla \rho \rangle_i^L) \cdot (\mathbf{r}_j - \mathbf{r}_i) \right] \frac{(\mathbf{r}_j - \mathbf{r}_i)}{\|\mathbf{r}_j - \mathbf{r}_i\|^2} \quad (3)$$

where $\langle \nabla \rho \rangle^L$ denotes the renormalized density gradient (Randles & Libersky 1996).

In Equation (2), p_{ij} is an artificial viscosity term employed to stabilize the WCSPH scheme, defined as

$$\pi_{ij} = \frac{(\mathbf{u}_j - \mathbf{u}_i) \cdot (\mathbf{r}_j - \mathbf{r}_i)}{\|\mathbf{r}_j - \mathbf{r}_i\|^2} \quad (4)$$

Equations (1) and (2) are not yet closed, and thus a linearized state equation is introduced:

$$p_i = c_0^2 (\rho_i - \rho_0) \quad (5)$$

Motion Equations of Moored Floating Structure

Following the Newton's second law, the translational and rotational motions of the structure are calculated by

$$M \frac{d\mathbf{E}}{dt} = \mathbf{F}_f + \mathbf{F}_m + M\mathbf{g} \quad (6)$$

$$I \frac{d\mathbf{\Theta}}{dt} = \mathbf{T}_f + \mathbf{T}_m \quad (7)$$

here, M , I , \mathbf{E} , and $\mathbf{\Theta}$ are the mass, moment of inertia, translational velocity, and rotational velocity of the structure, respectively. \mathbf{F}_f and \mathbf{F}_m are the fluid and mooring forces acting on the structure, respectively. \mathbf{T}_f and \mathbf{T}_m are the moments generated by \mathbf{F}_f and \mathbf{F}_m about the center of mass of the structure, respectively.

Fluid force

The solid boundaries are represented by three layers of dynamic boundary particles (Crespo et al. 2007). These particles, like fluid particles, participate in the calculations of Equations (1) and (5) to determine densities and pressures, respectively. However, they are not involved in the calculation of Equation (2) for velocity; instead, they either remain stationary or move with the solid body. The main drawback of dynamic boundary particles is the unrealistic absorption or repulsion of fluid particles at the solid boundary. To address this issue, the calculated densities of the dynamic boundary particles, obtained using Equation (1), are corrected as Cheng et al. (2021).

Based on Equation (2), the fluid force exerted on a dynamic boundary particle can be calculated by

$$\mathbf{f}_k = -\sum_i (p_i + p_k) \nabla_k W_{ki} V_i V_k + \alpha h c_0 \rho_0 \sum_i \pi_{ki} \nabla_k W_{ki} V_i V_k \quad (8)$$

\mathbf{F}_f and \mathbf{T}_f are then obtained as

$$\mathbf{F}_f = \sum_k \mathbf{f}_k \quad (9)$$

$$\mathbf{T}_f = \sum_k (\mathbf{r}_k - \mathbf{r}_c) \times \mathbf{f}_k \quad (10)$$

where \mathbf{r}_c is the position of the center of mass of the structure.

Mooring force

The mooring system is modelled as massless, linear elastic springs capable of bearing only tensile forces. Following the Hooke's law, \mathbf{F}_m

is calculated by

$$\mathbf{F}_m = \begin{cases} \mathbf{F}_{m0} + k_m (l_m - l_{m0}) \mathbf{g} & \text{if } l_m > l_{m0} \\ 0 & \text{if } l_m \leq l_{m0} \end{cases} \quad (11)$$

where \mathbf{F}_{m0} is the pre-tension; k_m is the coefficient of elasticity; l_m and l_{m0} are the real-time and initial lengths of the mooring line, respectively; \mathbf{g} is a unit vector pointing from the mooring position on the structure to the anchor position on the water bottom.

\mathbf{T}_m is then obtained as

$$\mathbf{T}_m = (\mathbf{r}_m - \mathbf{r}_c) \times \mathbf{F}_m \quad (12)$$

where \mathbf{r}_m is the mooring position on the structure.

Time-stepping Scheme

The explicit Symplectic scheme (Domínguez et al. 2022) with second-order computational accuracy is employed for time integration. The time step is variable and determined by the following equation:

$$\delta_t = \min \left[\begin{array}{l} 0.2 \min_i \left(\frac{h}{c_0 + h \max_j \pi_{ij}} \right), \\ 0.2 \min_i \left(\frac{h}{|D\mathbf{u}_i/Dt|} \right), 0.125 \frac{h^2}{\nu} \end{array} \right] \quad (13)$$

In Equation (13), the first term on the right-hand side represents the Courant-Friedrich-Lewy (CFL) condition with viscous control (Monaghan & Kos 1999), the second term limits the particle acceleration (Monaghan 1992), and the third term accounts for viscous diffusion (Morris et al. 1997).

MODEL VALIDATION

The convergence and accuracy of the established SPH model are validated through the numerical reproduction of a laboratory experiment. This section presents both the experimental and numerical setups, followed by a comparison of the numerical and experimental results.

Experimental and Numerical Setups

An experiment on wave interactions with a moored floating structure was conducted in a wave flume at Nagoya University (Peng et al. 2013), with dimensions of 30 m in length, 0.7 m in width, and 0.9 m in depth. Regular waves, characterized by a height (H) of 0.046 m, a period (T) of 1.0 s, and a wavelength (λ) of 1.538 m, were generated using an upstream wave paddle and dissipated by a downstream rubble mound. A cuboidal floating structure, measuring 0.4 m in length (L_f), 0.68 m in width, and 0.15 m in height (H_f), with $M = 28.6$ kg and $I = 0.435$ kg/m², was moored near the centre of the flume. $d = 0.6$ m, and the submersion depth (d_s) of the structure, measured from the still water level to its centroid, was 0.177 m. The mooring system comprised two high-stiffness chains on both the upwave and downwave sides, each forming a 60° angle with the flume bottom. Four wave gauges, labelled 1# to 4#, were mounted on both sides of the structure to measure wave elevations. Mooring forces were recorded using two load cells installed to the

chains. A laser system captured the kinematic response of the structure.

The simulation was performed in the 2D SPH wave flume, as depicted in Fig. 2. Identical waves were generated by an upstream piston-type active absorbing wavemaker and dissipated by a downstream sponge layer with a length of λ . Wave elevations were measured using wave gauges #1 to #4, positioned identically to the experimental setup in relation to the structure. Due to the dimensional difference between the 2D simulation and the 3D experiment, M and I of the numerical structure were adjusted to 42.06 kg and 0.64 kg·m², respectively, while L_f , H_f , d_s , d , and IMA remained unchanged. The high-stiffness chains were modelled with k_m set to 10⁶ N/m. To check the numerical convergence, three particle resolutions (H / δ_p) of 5, 10, and 15 were adopted.

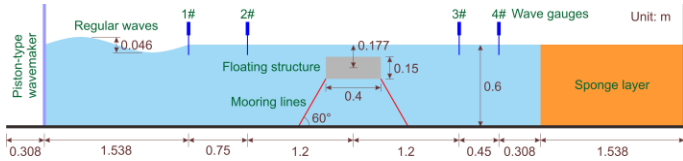


Fig. 2. Schematic of the numerical setup used to reproduce a laboratory experiment on regular wave interactions with a mooring floating structure

Comparisons of Numerical and Experimental Results

Fig. 3 shows the time histories of dimensionless wave elevations (η / H) at wave gauges 1# to 4# for different H / δ_p , comparing these results with experimental data. Satisfactory agreement is observed at wave gauges 1# to 3#. At wave gauge 4#, while the primary peak aligns well, the secondary peak is under-predicted. This discrepancy, as Ren et al. (2017) speculated, may be attributed to the artificial viscosity in Equation 2 which caused greater attenuation of high-frequency waves. Regarding numerical convergence, when H / δ_p increases from 5 to 10, the agreement at wave gauges 1# and 2# shows little change, but the predictions of double peaks at wave gauges 3# and 4# improves significantly. As H / δ_p increases further from 10 to 15, no noticeable improvement is observed across all wave gauges. These observations indicate that the established SPH model converges concerning numerical wave elevation, with $H / \delta_p = 10$ offering the optimal particle resolution, balancing both computational efficiency and numerical accuracy.

In Fig. 4, the dimensionless sway displacements (ξ_s / H), heave displacements (ξ_h / H), and roll angles ($\xi_r L_f / (2H)$) of the structure for different H / δ_p are compared with experimental data. Herein, a positive ξ_s corresponds to displacement in the direction of wave propagation, a positive ξ_h represents vertical upward movement, and a positive ξ_r means the structure tilts toward the incoming waves. Although the amplitude of ξ_s / H and the secondary valley of ξ_h / H are slightly under-predicted, the overall agreement remains satisfactory. Moreover, close numerical results are obtained for different H / δ_p , indicating that $H / \delta_p = 5$ is sufficient to capture the kinematic response of the structure. However, due to the higher requirement for numerical wave elevation, $H / \delta_p = 10$ is still necessary.

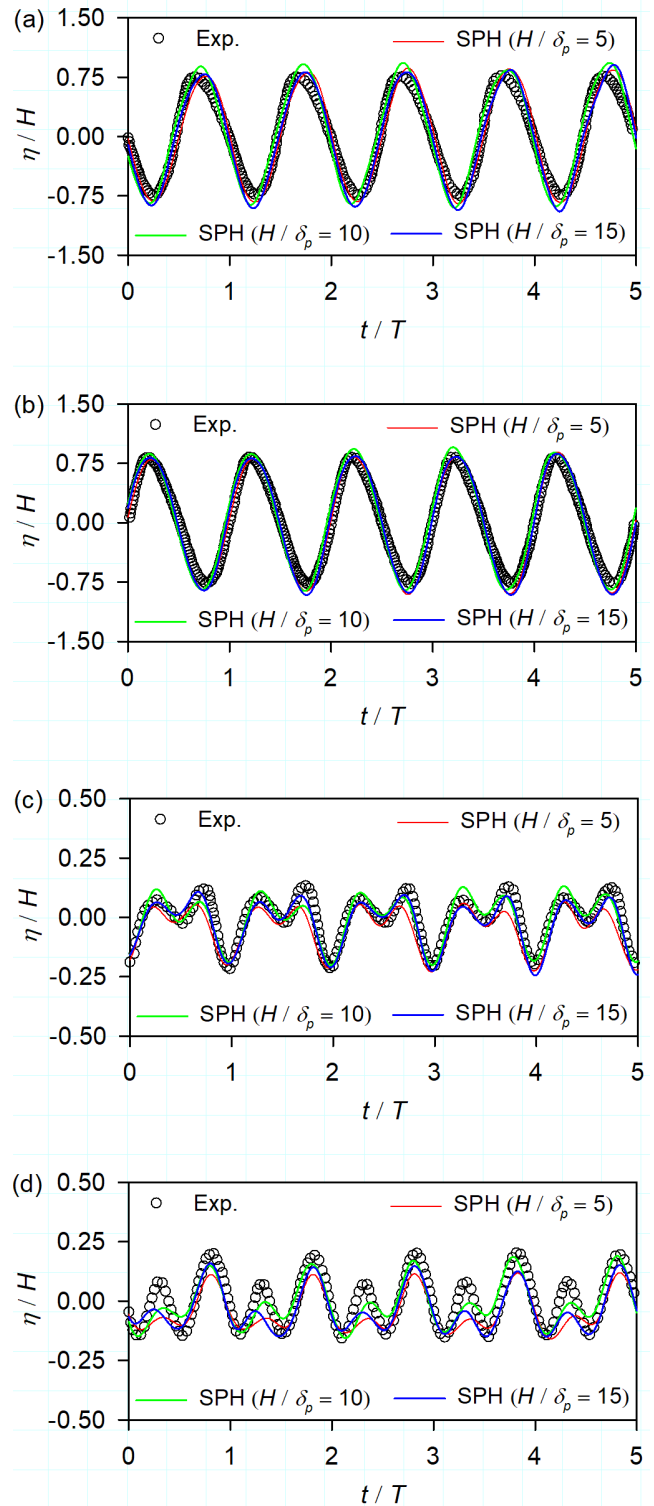


Fig. 3. Comparisons between the numerical and experimental wave elevations: (a) 1# wave gauge; (b) 2# wave gauge; (c) 3# wave gauge; (d) 4# wave gauge

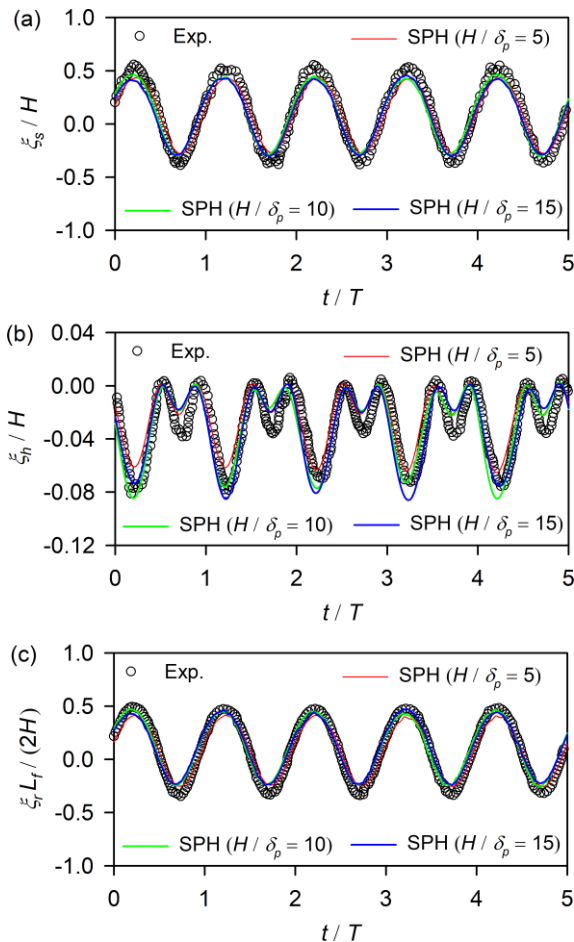


Fig. 4. Comparisons between the numerical and experimental kinematic responses: (a) sway displacements; (b) heave displacements; (c) roll angles

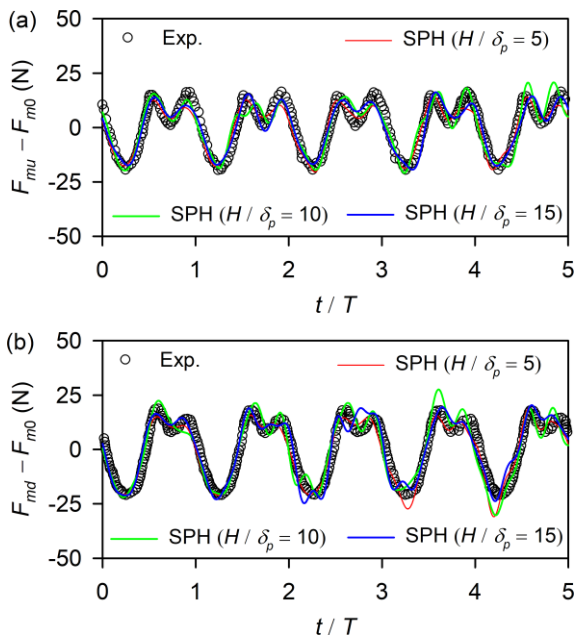


Fig. 5. Comparisons between the numerical and experimental dynamic mooring forces: (a) upwave side; (b) downwave side

Fig. 5 presents comparisons of the numerical and experimental dynamic mooring forces on the upward side ($F_{mu} - F_{m0}$) and downwave side ($F_{md} - F_{m0}$) of the structure. To account for the differences in dimensions and the number of mooring lines between the experiment and simulation, the numerical $F_{mu} - F_{m0}$ and $F_{md} - F_{m0}$ were adjusted prior to comparison. The numerical time history curves effectively reproduce the double-peak and single-valley features of the experimental data, with the first peak and the valley aligning closely, while the second peak is slightly under-predicted. Additionally, the numerical $F_{mu} - F_{m0}$ and $F_{md} - F_{m0}$ for $H / \delta_p = 5, 10,$ and 15 exhibit minimal differences and all closely agree with experimental data. Although the numerical time history curve for $H / \delta_p = 15$ is the most stable, $H / \delta_p = 10$ is preferred due to its superior computational efficiency.

N wave Generation by a Piston-type Wavemaker

Tadepalli and Synolakis (1996) described an N wave with an H in a water tank of d :

$$\eta(x, t) = \varepsilon \cdot (\theta - \kappa \cdot \delta) \cdot H \cdot \text{sech}^2(\theta) \quad (14)$$

where θ is defined as:

$$\theta = \kappa(x - ct - x_1) \quad (15)$$

In equation (14), ε is a scaling factor ensuring the wave height reaches the desired height H , $\delta = x_s - x_i$ is an eccentricity parameter, defined as the distance between $x = x_s$, the location of the inflection point of the wave profile at $t = 0$, thus $\eta(x_s, 0) = 0$, and $x = x_i$, the location at $t = 0$ of the crest of a solitary wave of the same height H and length λ (cf. Fig. 6). κ represents the generalized wavenumber, determined by the following equation:

κ represents the generalized wavenumber, determined by the following equation:

$$\kappa = \frac{1}{d} \sqrt{\frac{3H}{4d}} \quad (16)$$

The λ of the N wave is defined by the equation:

$$\lambda = \frac{2\pi}{k} \quad (17)$$

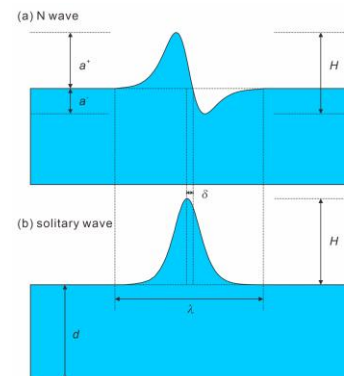


Fig. 6. N wave profile and corresponding solitary wave of the same height H and length λ .

Svendsen and Justesen (1984), following the reasoning of Goring and Raichlen (1980), assumed that the N wave has a permanent wave profile and a constant wave speed c , and derived the expression for an N wave with a permanent form:

$$\int_{-d}^{\eta} \mathbf{u} dz = \mathbf{c} \cdot \eta + Q_s + U_c \cdot d \quad (18)$$

Here, \mathbf{u} represents the particle velocity directly in front of the wavemaker, Q_s denotes the non-linear mass flux averaged over a wave period, and U_c is the current speed, defined as the average particle velocity beneath the wave trough level. For an infinitely long wave, the right-hand side of equation (18) simplifies to $\mathbf{c} \cdot \eta$ (Grilli and Svendsen, 1990). Since the piston motion generates a depth-uniform horizontal velocity $\mathbf{u} = \bar{\mathbf{u}}(t)$, equation (18) simplifies to:

$$\bar{\mathbf{u}} \cdot (d + \eta) = \mathbf{c} \cdot \eta \quad (19)$$

and thus, the particle velocity is given by

$$\bar{\mathbf{u}} = \frac{\mathbf{c} \cdot \eta}{d + \eta} \quad (20)$$

or in terms of the wavemaker's paddle velocity:

$$\frac{d\xi}{dt} = \frac{\mathbf{c} \cdot \eta}{d + \eta} \quad (21)$$

Here, $\xi(t)$ is the paddle trajectory, which can be obtained through integration of equation (21).

From Equation (21), an expression for the piston velocity can be obtained as:

$$\frac{d\xi}{dt} = \frac{\varepsilon H(\theta - \kappa\delta)c}{\varepsilon H(\theta - \kappa\delta) + d \cosh^2 \theta} \quad (22)$$

HYDRODYNAMIC BEHAVIOUR OF SFT

The validated SPH model is applied to analyse the hydrodynamic behaviour of an SFT under N wave action. This section details the numerical setup, motion response, and mooring force.

Numerical Setup

The interaction between a representative N wave and an SFT was simulated in the SPH wave flume, as depicted in Fig. 7. The N wave with $H = 30$ m was generated by a piston-type wavemaker. $d = 100$ m, and thus, under the Boussinesq assumption, λ was determined to be 1324.6 m. Despite full reflection occurring at the downstream end of the flume, the length of the flume was set to 3λ to ensure that the incident wave-SFT interaction was completed before any interference from the reflected wave. The SFT, featuring a circular CSS with a diameter of 40 m, was moored at the centre of the flume. $d_s = 30$ m, $\text{IMA} = 52.5^\circ$, and $k_m = 3.36 \times 10^6$ N/m. The BWR was set to 1.3, leading to $M = 9.67 \times 10^5$ kg and $F_{m0} = 1.79$ MN. Assuming M was uniformly distributed along the perimeter of the SFT, I was calculated to be 3.87×10^8 kg·m². A wave gauge was mounted at the location of the SFT

to measure the wave elevation. Based on the convergence check in the previous section, $H / \delta_p = 10$ was adopted, which gives $\delta_p = 3$ m for $H = 30$ m.

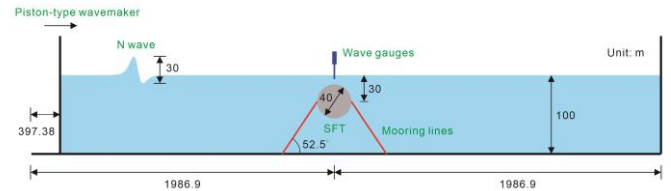


Fig. 7. Schematic of the numerical setup used to simulate the N wave interaction with an SFT

Motion Response and Mooring Force

Figs. 8 and 9 plot the time histories of (ξ_s, ξ_h, ξ_r) and (F_{mu}, F_{md}) induced by the N wave acting on the SFT. Four key moments are highlighted: t_0 denotes the initial moment at $t = 0$ s when wave generation begins; t_1 signifies the moment when the SFT reaches its maximum ξ_s in the direction of wave propagation; t_2 marks the moment when the SFT first returns to $\xi_s = 0$; t_3 corresponds to the moment of maximum ξ_s in the opposite direction of wave propagation. Fig. 10 displays the wave profiles, SFT postures, and mooring states at these four moments. The particles representing the SFT and the mooring system are coloured red, while the fluid particles are color-coded according to their pressures.

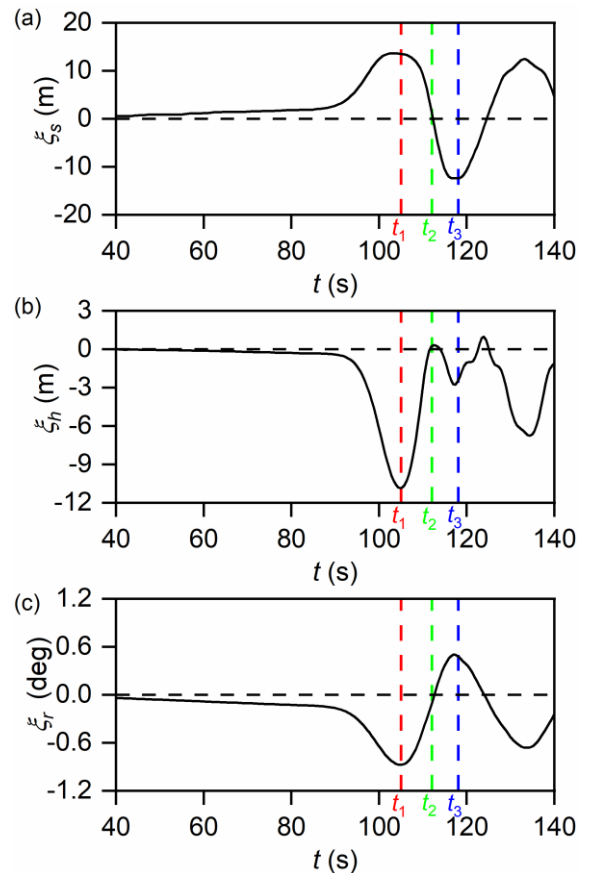


Fig. 8. Motion response of the SFT under N wave action: (a) sway displacement; (b) heave displacement; (c) roll angle. (t_0 at $t = 0$ s not shown)

As observed from Fig. 8 to 10, at moment t_0 , the water surface is calm and the SFT is in static equilibrium. As the wave approaches, the SFT begins to move in the direction of wave propagation. The mooring system restricts this movement, causing the SFT to descend and tilt toward the incoming wave. This motion results in an initial increase in F_{mu} followed by a decrease, while F_{md} decreases consistently. By moment t_1 , ξ_s reaches its maximum positive value, whereas ξ_h and ξ_r reach their maximum negative values. Simultaneously, both F_{mu} and F_{md} drop to local minima. As the wave passes, the SFT moves in the opposite direction of wave propagation. The asymmetry in the mooring system produces a restoring moment, causing the SFT to rotate toward the departing wave while it ascends. This motion leads to a general increase in both F_{mu} and F_{md} . At moment t_2 , ξ_s , ξ_h , and ξ_r approach zero, and both F_{mu} and F_{md} peak at nearly equal values. Subsequently, under the combined effects of residual wave force and inertia, the SFT continues moving in the opposite direction. Once more, the asymmetric mooring system forces the SFT to descend and tilt toward the departing wave. This motion reduces both F_{mu} and F_{md} , although fluctuations are observed during the reduction. By moment t_3 , ξ_s and ξ_h hit their maximum negative values, whereas ξ_r reaches its maximum positive value. At this point, both F_{mu} and F_{md} fall to zero. Throughout the entire wave-SFT interaction, the pressure field remains continuous and smooth.

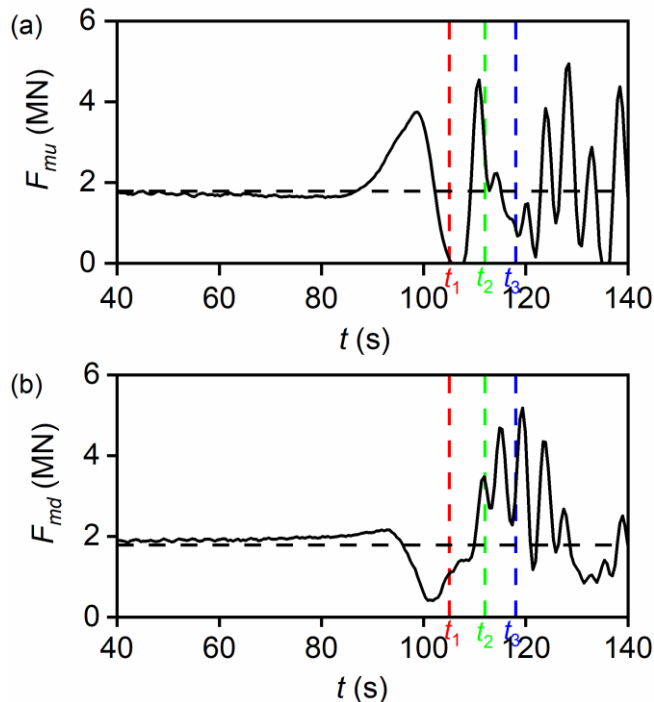


Fig. 9. Mooring force of the SFT under N wave action: (a) upwave mooring force; (b) downwave mooring force. (t_0 at $t = 0$ s not shown)

CONCLUSIONS

This study investigated the hydrodynamic behavior of SFTs under the action of a representative N wave. The interactions between the wave and the SFT were simulated using the SPH method, and the reliability of the method was validated by numerically reproducing laboratory experiments. Future research will compare the motion responses and mooring forces of submerged floating tunnels under N waves, solitary waves, and regular waves, as well as examine the dynamic responses of submerged floating tunnels with different design parameters.

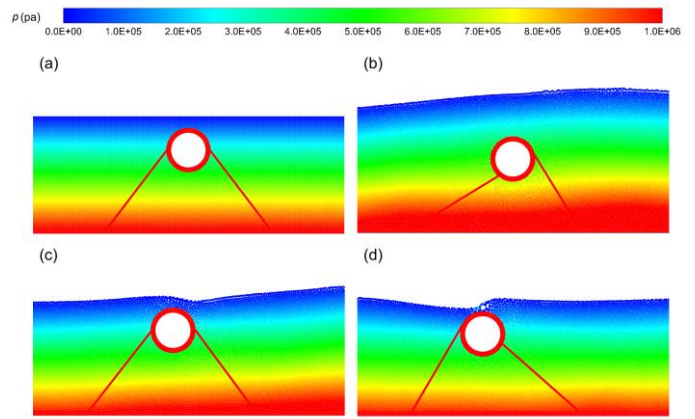


Fig. 10. Snapshots of N wave interaction with the SFT: (a) moment t_0 ; (b) moment t_1 ; (c) moment t_2 ; (d) moment t_3 .

ACKNOWLEDGEMENT

This work is supported by the National Natural Science Foundation of China (52131102), to which the authors are most grateful.

REFERENCES

- Antuono, M, Colagrossi, A, Marrone, S, et al. (2010). "Free-surface flows solved by means of SPH schemes with numerical diffusive terms," *Comput Phys Commun*, 181(3), 532–549.
- Chan, I-C, Liu, P L-F. (2012). "On the runup of long waves on a plane beach," *J. Geophys. Res.: Oceans*, 117, C08006.
- Chen, X, Chen, Q, Chen, Z, et al. (2021). "Numerical modeling of the interaction between submerged floating tunnel and surface waves," *Ocean Eng*, 220, 108494.
- Cheng, X, Liu, C, Zhang, Q, et al. (2021). "Numerical study on the hydrodynamic characteristics of a double-row floating breakwater composed of a pontoon and an airbag," *J Mar Sci Eng*, 9(9), 983.
- Crespo, AJC, Gómez-Gesteira, M, and Dalrymple, RA (2007). "Boundary conditions generated by dynamic particles in SPH methods," *Comput Mater Continua*, 5(3), 173–184.
- Domínguez, JM, Fourtakas, G, Altomare, C, et al. (2022). "DualSPHysics: from fluid dynamics to multiphysics problems," *Comput Part Mech*, 9(5), 867–895.
- Faggiano, B, Panduro, J, Rosas, MTM, et al. (2016). "The conceptual design of a roadway SFT in Baja California, Mexico," *Procedia Eng*, 166, 3–12.
- Fogazzi, P, and Perotti, F (2000). "The dynamic response of seabed anchored floating tunnels under seismic excitation," *Earthq Eng Struct Dyn*, 29(3), 273–295.
- Goring, D, and Raichlen, F (1980). "The generation of long waves in the laboratory," *Proc 17th Conf Coast Eng*, Sydney, ASCE, 763–783.
- Goseberg, N, Wurpts, A, Schlurmann, T. (2013). "Laboratory-scale generation of tsunami and long waves," *Coast. Eng.*, 79, 57–74.
- Grilli, S, and Svendsen, IA (1990). "Computation of nonlinear wave kinematics during propagation and runup on a slope," In: Tørum, A, and Gudmestad, OT (Eds.), *Water Wave Kinematics*, NATO ASI Series E178, Kluwer Academic Publishers, The Netherlands, 387–412.
- He, M, Gao, X, Xu, W, et al. (2019). "Potential application of submerged horizontal plate as a wave energy breakwater: A 2D study using the WCSPH method," *Ocean Eng*, 185, 27–46.
- He, M, Khayyer, A, Gao, X, et al. (2021). "Theoretical method for

- generating solitary waves using plunger-type wavemakers and its Smoothed Particle Hydrodynamics validation," *Appl Ocean Res*, 106, 102414.
- Kanie, S (2010). "Feasibility studies on various SFT in Japan and their technological evaluation," *Procedia Eng*, 4, 13–20.
- Kunisu, H (2010). "Evaluation of wave force acting on Submerged Floating Tunnels," *Procedia Eng*, 4, 99–105.
- Larssen, RM, and Jakobsen, SE (2010). "Submerged floating tunnels for crossing of wide and deep fjords," *Procedia Eng*, 4, 171–178.
- Liang, D, Gotoh, H, Khayyer, A, et al. (2013). "Boussinesq modelling of solitary wave and N-wave runup on coast," *Appl Ocean Res*, 42, 144–154.
- Liang, D, Jian, W, Shao, S, et al. (2017). "Incompressible SPH simulation of solitary wave interaction with movable seawalls," *J Fluids Struct*, 69, 72–88.
- Lima, VV, Avilez-Valente, P, Baptista, MV, and Miranda, JM (2019). "Generation of N-waves in laboratory," *Coastal Eng*, 148, 1–18.
- Lo, H-Y, and Liu, PL-F (2014). "Solitary waves incident on a submerged horizontal plate," *J Waterw Port Coast Ocean Eng*, 140(3).
- Luo, G, Pan, S, Zhang, Y, et al. (2019). "Response analysis of submerged floating tunnel hit by submarine based on Smoothed-Particle Hydrodynamics," *Shock Vib*, 2019, 1–12.
- Lynett, PJ, Liu, PL-F, Losada, IJ, et al. (2000). "Solitary wave interaction with porous breakwaters," *J Waterw Port Coast Ocean Eng*, 126(6), 314–322.
- Madsen, P A, Fuhrman, D R, Schäffer, H A. (2008). "On the solitary wave paradigm for tsunamis," *J. Geophys. Res.: Oceans*, 113(C12).
- Monaghan, JJ (1992). "Smoothed particle hydrodynamics," *Annu Rev Astron Astrophys*, 30(1), 543–574.
- Monaghan, JJ, and Kos, A (1999). "Solitary waves on a Cretan beach," *J Waterw Port Coast Ocean Eng*, 125(3), 145–155.
- Morris, JP, Fox, PJ, and Zhu, Y (1997). "Modeling low Reynolds number incompressible flows using SPH," *J Comput Phys*, 136(1), 214–226.
- Paik, IY, Oh, CK, Kwon, JS, et al. (2004). "Analysis of wave force induced dynamic response of submerged floating tunnel," *KSCE J Civ Eng*, 8(5), 543–550.
- Peng, W, Lee, K-H, Shin, S-H, et al. (2013). "Numerical simulation of interactions between water waves and inclined-moored submerged floating breakwaters," *Coastal Eng*, 82, 76–87.
- Ran, Q, Tong, J, Shao, S, et al. (2015). "Incompressible SPH scour model for movable bed dam break flows," *Adv Water Resour*, 82, 39–50.
- Randles, PW, and Libersky, LD (1996). "Smoothed Particle Hydrodynamics: Some recent improvements and applications," *Comput Methods Appl Mech Eng*, 139(1–4), 375–408.
- Schmidt-Koppenhagen, R, Grüne, J, and Oumeraci, H (2006). "Tsunami wave decay in near- and onshore areas," *Proc 30th Conf Coast Eng*, San Diego, World Scientific, 1664–1676.
- Seo, S, Mun, H, Lee, J, et al. (2015a). "Simplified analysis for estimation of the behavior of a submerged floating tunnel in waves and experimental verification," *Mar Struct*, 44, 142–158.
- Seo, S, Sagong, M, and Son, S (2015b). "Global response of submerged floating tunnel against underwater explosion," *KSCE J Civ Eng*, 19(7), 2029–2034.
- Svendsen, IA, and Justesen, P (1984). "Forces on slender cylinders from very high and spilling breakers," *Proc Symp Description and Modelling of Directional Seas*, Paper D-7-1, Technical University of Denmark, 16 pp.
- Synolakis, CE, and Skjelbreia, JE (1993). "Evolution of maximum amplitude of solitary waves on plane beaches," *J Waterw Port Coast Ocean Eng*, 119, 323–342.
- Tadepalli, S, and Synolakis, CE (1996). "Model for the leading waves of tsunamis," *Phys Rev Lett*, 77, 2141–2144.
- Wang, L, Xu, M, Zhang, C, et al. (2023). "Numerical investigation on solitary waves traveling over rigid vegetation by a 3D-MPS method," *Appl Ocean Res*, 132, 103476.
- Wendland, H (1995). "Piecewise polynomial, positive definite and compactly supported radial functions of minimal degree," *Adv Comput Math*, 4(1), 389–396.
- Xiang, Y, Chen, Z, Yang, Y, et al. (2018). "Dynamic response analysis for submerged floating tunnel with anchor-cables subjected to sudden cable breakage," *Mar Struct*, 59, 179–191.
- Yang, Z, Li, J, Zhang, H, et al. (2020). "Experimental study on 2D motion characteristics of submerged floating tunnel in waves," *J Mar Sci Eng*, 8(2), 123.
- Zhang, B, Ye, J, Zhou, H, et al. (2024). "Enhancing tsunami modelling by using N-waves and the measured topography of coral reef: A study in the South China Sea," *Coastal Engineering*, 193, 104601.